ICON-HAM-lite 1.0: simulating the Earth system with interactive aerosols at kilometer scales

Philipp Weiss[1], Ross Herbert[2], and Philip Stier[1]

[1]Department of Physics, University of Oxford, United Kingdom
[2]School of Earth and Environment, University of Leeds, United Kingdom

Correspondence: Philipp Weiss (philipp.weiss@physics.ox.ac.uk)

Abstract. Aerosols strongly influence Earth's climate as they scatter and absorb radiation and serve as condensation nuclei for cloud droplets and ice particles. New Earth system models that run at kilometer resolutions allow us to examine long-standing questions related to these interactions. To perform kilometer-scale simulations with the Earth system model ICON-MPIM, we developed the one-moment aerosol module HAM-lite. HAM-lite was derived from the two-moment module HAM. Like in HAM, aerosols are represented as an ensemble of log-normal modes. Unlike in HAM, aerosol sizes and compositions are prescribed, which reduces the computational costs significantly. Here, we present a first global simulation with four aerosol modes at a resolution of five kilometers and over a period of one year. The simulation captured key aerosol processes including, for example, the emission of dust aerosols by convective storms in the Sahara and the interactions between sea salt aerosols and tropical cyclones in the Pacific.

1 Introduction

Aerosols originate from natural processes, including dust storms and sea spray, but also from human activities, including fuel combustion or biomass burning. They influence the climate directly by scattering or absorbing radiation and indirectly by acting as cloud condensation nuclei or ice nucleating particles (Boucher et al., 2013). According to Forster et al. (2021), the effective radiative forcing over the industrial era (1750 to 2014) is $-0.3\,[-0.6$ to $0.0]\ \mathrm{W\,m^{-2}}$ due to aerosol-radiation interactions and $-1.0\,[-1.7$ to $-0.3]\ \mathrm{W\,m^{-2}}$ due to aerosol-cloud interactions. The uncertainties of these estimates have reduced over the past years but are still relatively large reflecting the complexity of the underlying processes (Thornhill et al., 2021).

Earth system models have improved our understanding of aerosols, radiation, and clouds significantly. Current models simulate the Earth system including interactive aerosols at horizontal resolutions of about 100 kilometers. Due to their low resolution, such models can run with complex microphysics and chemistry over long periods of many centuries (Thornhill et al., 2021). However, important small-scale processes such as aerosol-convection interactions are not resolved but parameterized. Next-generation models simulate the Earth system with horizontal resolutions below 10 kilometers and are capable of capturing processes like deep convective updrafts in the atmosphere or mesoscale eddies in the ocean. Due to the high computational demand, such models run with simple microphysics over short periods of several decades. And in almost all models, aerosols are not interactive but prescribed based on previous observations (Prein et al., 2015; Stevens et al., 2019).

25 To simulate the Earth system with interactive aerosols at kilometer scales, we developed the one-moment aerosol module HAM-lite based on the two-moment module HAM (Stier et al., 2005; Zhang et al., 2012; Salzmann et al., 2022). Like in HAM, aerosols are represented as an ensemble of log-normal modes. Unlike in HAM, aerosol sizes and compositions are prescribed. With that, we only need prognostic tracers for aerosol concentrations. And in turn, we keep the computational costs related to aerosols small and make simulations at fine resolutions and over multiple years possible. Here, we present a first simulation

30 with ICON-MPIM (Hohenegger et al., 2023) coupled to HAM-lite at a resolution of five kilometers and over a period of one year. We provide an overview of the global aerosol cycle and insights into regional processes that unfold at kilometer scales.

The paper is structured as follows. In section 2, we describe the aerosol module HAM-lite including its modal structure and interactive processes. In section 3, we describe the simulation setup and computational procedure. In section 4, we present an initial analysis of the simulation. And in section 5, we summarize the current state of HAM-lite and provide an outlook for

35 future developments.

2   Model description

In HAM-lite, the aerosols are represented by an ensemble of log-normal modes. The microphysical interactions of aerosols are prescribed such that the mean radius and standard deviation of a mode are constant. The selection of modes is flexible. A mode can be within the nucleation, Aitken, accumulation, or coarse range, i.e., the mean radius can range from below

40 $0.005\,\mu\mathrm{m}$ to above $0.5\,\mu\mathrm{m}$. And a mode can be composed of internal mixtures of dust, sea salt, black carbon, organic carbon, or sulfate, i.e., all particles within a mode consist of the same mixture of species (Riemer et al., 2019). The calculation of aerosol properties, which govern processes like sedimentation or wet deposition, remains consistent with HAM. The modes of HAM-lite interact with the processes of ICON-MPIM, i.e., aerosols are transported as tracers in its dynamical core and are coupled to its parameterization schemes.

2.1   Aerosol modes

The size distribution of aerosols can be approximated as a superposition of log-normal modes

$$N\left(\ln r\right)=\sum_{j=1}^{J}\frac{N_j}{\sqrt{2\pi}\ln\sigma_j}\exp\left(-\frac{\left(\ln r-\ln\overline{r}_j\right)^2}{2\ln^2\sigma_j}\right),\tag{1}$$

in which J is the number of modes (Seinfeld and Pandis, 2016). Each mode is defined by three moments, i.e., the particle number N_j, number median radius $\overline{r}_j$, and standard deviation σ_j. In the two-moment scheme HAM, the particle number and

50 mean radius are variable, whereas the standard deviation is prescribed. A particle in a mode j is composed of different species k with masses $M_{j,k}$, which vary due to microphysical processes such as coagulation or condensation. In the default modal structure of HAM, there are four hydrophilic and three hydrophobic modes in the nucleation, Aitken, accumulation, and coarse range. The particles are composed of internal mixtures of five species, i.e., dust, sea salt, sulfate, organic carbon, and black carbon. In a climate simulation, the particle numbers and masses are represented as prognostic tracers (Salzmann et al., 2022).

Table 1. A possible configuration of aerosol modes in HAM-lite.

Size range (μm)	Aerosol mode
Nucleation ($\overline{r} \leq 0.005$)	
Aitken ($0.005 < \overline{r} \leq 0.05$)	
Accumulation ($0.05 < \overline{r} \leq 0.5$)	N_1, N_2
Coarse ($0.5 < \overline{r}$)	N_3, N_4

55 The transport of prognostic tracers requires significant computational resources such that global simulations with HAM are only feasible at coarse resolutions larger than 10 kilometers. In order to make global simulations at fine resolutions smaller than 10 kilometers possible, we reduce the physical complexity of HAM and develop the one-moment scheme HAM-lite. First, we prescribe the mean radius and particle composition such that we only need prognostics tracers for particle numbers. And second, we represent only hydrophilic modes such that we can further reduce the number of prognostic tracers to about

60 three to five. In HAM-lite, a particle in a mode j is composed of different species k with constant volume fractions $\alpha_{j,k}$. The properties of a particle are computed as volume-weighted averages over the properties of the individual species. The density ρ_j and hygroscopicity parameter κ_j of a particle are therefore

$$\rho_j = \sum_{k=1}^{K} \alpha_{j,k}\rho_k \quad \text{and} \quad \kappa_j = \sum_{k=1}^{K} \alpha_{j,k}\kappa_k, \tag{2}$$

in which ρ_k and κ_k are the density and hygroscopicity of species k. Based on the number median radius and hygroscopicity,

65 the wet radius and density of a particle are computed as a function of the air temperature T and relative humidity RH,

$$\overline{r}_{\mathrm{w},j} = f_{\mathrm{g}}(T, RH, \overline{r}_j, \kappa_j)\overline{r}_j \tag{3}$$

and

$$\rho_{\mathrm{w},j} = (\rho_j V_j + \rho_{\mathrm{wa}} V_{j,\mathrm{wa}})/V_{\mathrm{w},j}, \tag{4}$$

in which f_{g} is the hygroscopic growth factor from Petters and Kreidenweis (2007), V_j is the dry volume, $V_{j,\mathrm{wa}} = V_{\mathrm{w},j} - V_j$ is

70 the water volume, and ρ_{wa} is the water density. Note that the dry and wet volumes are computed based on the radius of average mass, that is, $\overline{r}_{\mathrm{m},j} = \exp((3/2)\ln^2 \sigma_j)\overline{r}_j$ (Hinds and Zhu, 1982). Since the composition and size of a particle are prescribed, we can tabulate the wet radius and density once at the initialisation stage as a function of the air temperature and relative humidity.

 The modal structure of HAM-lite is flexible. The number, size, and composition of modes can be chosen according to the computational resources and research question. Table 1 shows a possible configuration with four hydrophilic modes in the

75 accumulation and coarse range.
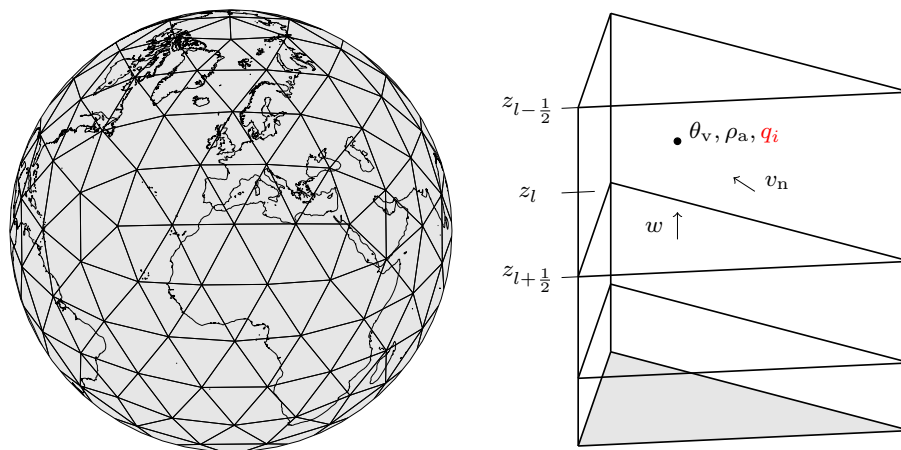
Figure 1. Spatial discretization and prognostic variables: icosahedral grid with equilateral triangles (left) and vertical column with full and half levels (right). Prognostic tracers that belong to the cloud or aerosol scheme are highlighted in red.

2.2 Atmospheric processes

The prognostic tracers that represent aerosols are transported through the atmosphere and influenced by various processes such as convection or precipitation. Figure 1 shows the prognostic variables and their spatial discretization in the Earth system model ICON-MPIM. The prognostic variables are the virtual temperature θ_v, air density ρ_a, horizontal and vertical velocities v_n and w, and tracers q_i. The tracers represent mixing ratios of water species or aerosols with respect to air mass. Horizontally, the atmosphere is discretized with an icosahedral-triangular C grid. Vertically, the atmosphere is divided into levels based on terrain-following coordinates (Giorgetta et al., 2018; Hohenegger et al., 2023).

Small-scale processes within a grid cell need to be parameterized. These paramaterized processes impose tendencies on the prognostic variables. There are three parameterization schemes for cloud microphysics, radiation, and turbulence as shown in figure 2 adapted from Hohenegger et al. (2023). Cloud microphysics are parametrized with the one-moment scheme from Baldauf et al. (2011). The scheme computes specific masses of six water classes, i.e., water vapour, cloud water, cloud ice, rain, snow, and graupel. The cloud droplet number and ice particle number are not prognostic but diagnosed. Radiation is parameterized with the radiative transfer scheme from Pincus et al. (2019). The scheme computes radiative properties and fluxes over 14 shortwave bands and 16 longwave bands. As shown in figure 2, it is called less frequently than the other schemes due to its computational complexity. Lastly, the turbulence is parametrized with the Smagorinsky scheme implemented by Dipankar et al. (2015). Surface fluxes are computed in coordination with the land scheme JSBACH from Reick et al. (2021). Note that there is no convection scheme even though turbulent eddies are only partially resolved at kilometer scales.
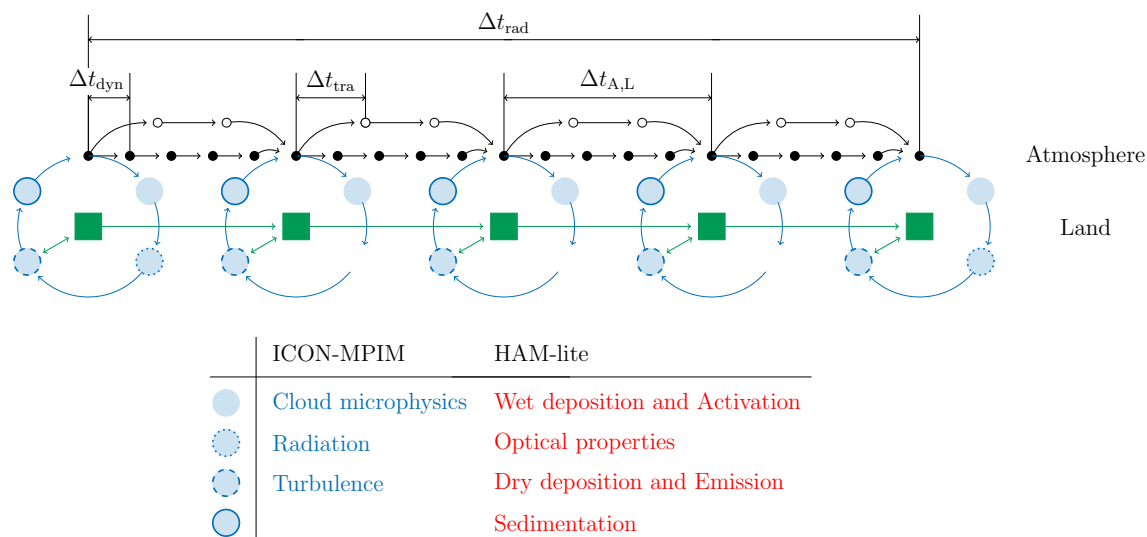
Figure 2. Time stepping (top) and parameterized processes (bottom): dynamical core and tracer transport (black), parameterized processes (blue), and land scheme (green). Processes of ICON-MPIM are highlighted in blue, and processes of HAM-lite are highlighted in red.

2.3 Aerosol processes

The aerosol module interacts with these processes, for example, when cloud droplets form on aerosol particles or surface winds
95 drive dust emissions. Figure 2 shows how the parameterization schemes of ICON-MPIM and HAM-lite are coupled to each other (Salzmann et al., 2022). Wet deposition and activation are linked to the cloud microphysics scheme, radiative properties of aerosols are factored into the radiation scheme, and dry deposition and emission are linked to the turbulence scheme. Sedimentation is called separately at the end of the cycle. In the next sections, we introduce the different schemes of HAM-lite. The schemes impose either surface fluxes ($\mathrm{m}^{-2}\,\mathrm{s}^{-1}$) or tendencies ($\mathrm{kg}^{-1}\,\mathrm{s}^{-1}$) on the aerosol tracers, which represent aerosol
100 number per air mass (kg^{-1}). In order to simplify the notation, the indices of full and half levels, i.e., z_l and $z_{l\pm1/2}$, are omitted.

2.3.1 Emission

Emissions are computed interactively or prescribed based on emission scenarios. Sea salt emissions are imposed as surfaces fluxes and computed based on a scheme of Gong (2003), taking into account the surface wind speed and sea surface temperature. Dust emissions are also imposed as surfaces fluxes and computed based on a scheme of Tegen et al. (2019), taking into
105 account the surface wind speed and various surface properties provided by the land scheme. The emissions of sulfate, organic carbon, and black carbon are imposed as surfaces fluxes or tendencies and taken from the AeroCom-II ACCMIP database (Heil et al., 2022). It provides monthly averages of emissions from anthropogenic sources and biomass burning (Salzmann et al., 2022). The emissions are grouped into emission sectors such as forest fires or energy production. The emission sectors are attributed to different aerosol modes. To forward emissions to modes, the mass fluxes from the database are converted into

number fluxes

$$F_{\text{em},j,k,s} = \frac{3}{4\pi \overline{r}_{\text{m},j}^3 \rho_k} S_{\text{em},k,s}, \tag{5}$$

where $S_{\text{em},k,s}(z)$ is the mass flux of species k in sector s. Note that the mass fluxes from the dust and sea salt emission schemes are converted in the same manner. The number fluxes are then added together such that the total number flux reads

$$F_{\text{em},j} = \sum_{k=1}^{K} \sum_{s=1}^{S} F_{\text{em},j,k,s}, \tag{6}$$

where S is the number of sectors that belong to the mode. The composition of a mixed mode with prescribed emissions can be derived from its number fluxes. The volume fraction of species j in mode k reads

$$\alpha_{j,k} = \frac{\sum_{s=1}^{S} N_{\text{em},j,k,s}}{\sum_{k=1}^{K} \sum_{s=1}^{S} N_{\text{em},j,k,s}}, \tag{7}$$

where $N_{\text{em},j,k,s}$ is the total number of particles emitted over the simulation period. Since the number fluxes are prescribed, the volume fractions can be computed once at the initialization stage.

2.3.2 Sedimentation

The sedimentation tendency is computed on all levels throughout the column as

$$F_{\text{se},j} = q_j v_{\text{se},j}/\Delta z, \tag{8}$$

in which q_j is the number mixing ratio, $v_{\text{se},j}$ is the sedimentation velocity, and $\Delta z = z_{l+1} - z_l$ is the distance between two full levels. The sedimentation velocity is modeled based on Stokes theory (Seinfeld and Pandis, 2016), i.e.,

$$v_{\text{se},j} = \frac{2}{9} \frac{g\left(\rho_{\text{w},j} - \rho_{\text{a}}\right) r_{\text{w},j}^2}{\mu_{\text{a}}}$$
$$\left(\exp\left(2\ln^2 \sigma_j\right) + 1.246 \frac{\lambda_{\text{a}}}{\overline{r}_{\text{w},j}} \exp\left(\frac{\ln^2 \sigma_j}{2}\right) \right), \tag{9}$$

in which g is the gravitational acceleration and λ_{a} is the mean free path. The term on the second line accounts for non-continuum effects following Riemer (2002). To ensure numerical stability, the velocity is limited to $\Delta z/\Delta t_{\text{A,L}}$. Note that sedimentation to the surface is handled by the dry deposition scheme introduced in the next section.

2.3.3 Dry deposition

The dry deposition flux to the surface is computed as

$$F_{\text{dd},j} = \rho_{\text{a}} q_j v_{\text{dd},j}, \tag{10}$$

in which $v_{\text{dd},j}$ is the dry deposition velocity. It is formulated based on the scheme of Pleim et al. (2022), i.e.,

$$v_{\text{dd},j} = \frac{v_{\text{se},j}}{1 - \exp\left(-v_{\text{se},j}\left(R_{\text{ar}} + R_{\text{ls},j}\right)\right)} \tag{11}$$

in which R_{ar} is the aerodynamic resistance and $R_{\mathrm{sf},j}$ is the laminar sublayer resistance. The aerodynamic resistance reads

$$R_{\mathrm{ar}} = \frac{1}{c_\kappa u_*} \left(\ln \left(\frac{z_{\mathrm{sf}}}{z_0} \right) - \Psi_{\mathrm{H}} \right), \tag{12}$$

in which the von Karman constant c_κ, friction velocity u_*, and similarity profile $(\ln(z_{\mathrm{sf}}/z_0) - \Psi_{\mathrm{H}})$ are taken from the turbulence scheme of ICON-MPIM (Dipankar et al., 2015). The laminar sublayer resistance reads

$$R_{\mathrm{ls},j} = \frac{1}{\epsilon_{\mathrm{ls}} u_* (E_{\mathrm{bd},j} + E_{\mathrm{im},j})}, \tag{13}$$

in which the ϵ_{ls} is an empirical correction and $E_{\mathrm{bd},j}$ and $E_{\mathrm{im},j}$ are collection efficiencies due to Brownian diffusion and impaction. The empirical correction is equal to one for non-vegetated surfaces and equal to the leaf area index for vegetated surfaces. The vegetation fraction and leaf area index are provided by the land scheme. The collection efficiencies depend on the Stokes and Schmidt numbers. The Schmidt number reads $Sc = \nu_{\mathrm{a}}/D_j$, in which ν_{a} is the kinematic viscocity of air and

$$D_j = \frac{k_{\mathrm{B}} T_{\mathrm{a}}}{6\pi \mu_{\mathrm{a}} \overline{r}_{\mathrm{w},j}}$$

$$\left(\exp \left(\frac{\ln^2 \sigma_j}{2} \right) + 1.246 \frac{\lambda_{\mathrm{a}}}{\overline{r}_{\mathrm{w},j}} \exp \left(2\ln^2 \sigma_j \right) \right) \tag{14}$$

is the diffusion coefficient. Like the sedimentation velocity, it is corrected for non-continuum effects following Riemer (2002). The Stokes number reads $St_j = \rho_{\mathrm{a}} v_{\mathrm{se},j} u_*^2 / (g\mu_{\mathrm{a}})$ for non-vegetated surfaces and $St_j = v_{\mathrm{se},j} u_* / (g A_{\mathrm{co}})$ for vegetated surfaces, in which A_{co} is the characteristic size of collectors like leafs or needles. It is assumed to be $10\,\mathrm{mm}$ for of macroscale collectors and $1\,\mu\mathrm{m}$ for microscale collectors. To ensure numerical stability, the dry deposition velocity is limited to $\Delta z_{\mathrm{sf}}/\Delta t_{\mathrm{A,L}}$, where Δz_{sf} is the thickness of the surface layer and $\Delta t_{\mathrm{A,L}}$ is the time step of the atmosphere and land as show in figure 2. The dry deposition flux is subtracted from the emission flux such that a net surface flux is returned to the turbulence scheme as indicated in figure 2.

2.3.4 Wet deposition

The wet deposition tendency is computed for all cloudy levels throughout the column as

$$F_{\mathrm{wd},j} = q_j f_{\mathrm{ac},j}(z_{\mathrm{cb}}) \frac{q_{\mathrm{ra}} + q_{\mathrm{gr}} + q_{\mathrm{sn}}}{q_{\mathrm{cw}} + q_{\mathrm{ci}} + q_{\mathrm{ra}} + q_{\mathrm{gr}} + q_{\mathrm{sn}}}$$

$$\frac{p_{\mathrm{ra}} + p_{\mathrm{gr}} + p_{\mathrm{sn}}}{\int (q_{\mathrm{ra}} + q_{\mathrm{gr}} + q_{\mathrm{sn}}) \rho_{\mathrm{a}} dz}, \tag{15}$$

in which $f_{\mathrm{ac},j}$ is the fraction of activation at cloud base z_{cb}, q_{cw}, q_{ci}, q_{ra}, q_{gr}, and q_{sn} are the mass mixing ratios of cloud water, cloud ice, rain, graupel, and snow, and p_{ra}, p_{gr}, and p_{sn} are the precipitation rates of rain, graupel, and snow. The first term is the number of aerosols activated at cloud base. The second term on the first line is the ratio of the precipitating water classes and condensed water classes. It incorporates the fraction of condensed water that forms precipitation. And the third term on the second line is the ratio of the total surface precipitation and column integral over the precipitating water classes. It incorporates the fraction of precipitation that reaches the surface. A grid cell is assumed to be cloudy, if its cloud water and ice is larger than $10^{-6}\,\mathrm{kg\,kg^{-1}}$. Note that the same threshold is used in the cloud microphysics scheme itself (Baldauf et al., 2011).

2.3.5 Activation

165 The fraction of activation is calculated with a scheme of Abdul-Razzak and Ghan (2000) based on the updraft velocity, wet diameter, and various other quantities. The activated particles of the different modes are then added together to obtain the cloud droplet number concentration

$$N_{\mathrm{cd}} = \sum_{j=1}^{J} \rho_{\mathrm{a}}(z_{\mathrm{cb}}) q_j(z_{\mathrm{cb}}) f_{\mathrm{ac},j}(z_{\mathrm{cb}}). \tag{16}$$

Due to the limited resolution of a few kilometers, convective updrafts are only partially resolved. To account for that, the
170 minimum number concentration is set to $30\,\mathrm{cm}^{-3}$ similarly to Goto et al. (2020) who used a lower bound of $25\,\mathrm{cm}^{-3}$. An alternative would be to implement a scheme for the unresolved updrafts as outlined by Malavelle et al. (2014). Note that the number concentration is used to calculate the autoconversion rate in the cloud microphysics scheme and the cloud optics in the radiation scheme (Seifert and Beheng, 2006; Pincus et al., 2019).

2.3.6 Optical properties

175 The aerosol optical properties are calculated on all levels according to Mie theory (Stier et al., 2005, 2007). They are extracted from look-up tables based on the standard deviation σ_j, Mie size parameter $X_j = 2\pi\overline{r}_{\mathrm{w},j}/\lambda$, and refractive index $\boldsymbol{n}_j = n_{\mathrm{real},j} + \mathrm{i}\,n_{\mathrm{imag},j}$. Similar to the other particle properties, the real and imaginary parts of the refractive index are computed as volume-weighted averages over the individual species including water such that

$$n_{\mathrm{real},j} = \frac{\sum_{k=1}^{K} V_{j,k} n_{\mathrm{real},k} + V_{j,\mathrm{wa}} n_{\mathrm{real},\mathrm{wa}}}{\sum_{k=1}^{K} V_{j,k} + V_{j,\mathrm{wa}}} \tag{17}$$

180 and

$$n_{\mathrm{imag},j} = \frac{\sum_{k=1}^{K} V_{j,k} n_{\mathrm{imag},k} + V_{j,\mathrm{wa}} n_{\mathrm{imag},\mathrm{wa}}}{\sum_{k=1}^{K} V_{j,k} + V_{\mathrm{wa},j}}. \tag{18}$$

The extinction coefficient $C_{\mathrm{ext},j}$, single scattering albedo $C_{\mathrm{ssa},j}$, and assymetry factor $C_{\mathrm{asy},j}$ of the different modes are then combined to get bulk optical properties, i.e.,

$$C_{\mathrm{ext}} = \sum_{j=1}^{J} N_j C_{\mathrm{ext},j}, \tag{19}$$

185 $$C_{\mathrm{ssa}} = \frac{\sum_{j=1}^{J} N_j C_{\mathrm{ext},j} C_{\mathrm{ssa},j}}{C_{\mathrm{ext}}}, \tag{20}$$

and

$$C_{\mathrm{asy}} = \frac{\sum_{j=1}^{J} N_j C_{\mathrm{ext},j} C_{\mathrm{ssa},j} C_{\mathrm{asy},j}}{C_{\mathrm{ext}} C_{\mathrm{ssa}}}, \tag{21}$$

in which $N_j = \rho_{\mathrm{a}} q_j \Delta z$ is the aerosol number in layer Δz. Note that the extinction coefficient is computed on longwave and shortwave bands, whereas the single scattering albedo and asymmetry factor are computed only on shortwave bands (Bohren
190 and Huffman, 1998; Siebesma et al., 2020).

Table 2. Aerosol composition and properties. Volume fractions (α_k) were derived from AeroCom-II ACCMIP (Heil et al., 2022). Number median radii ($\overline{r}$) were adapted from MACv2 (Kinne, 2019). Densities (ρ) and hygroscopicities (κ) of species were taken from ECHAM6.3-HAM2.3 (Tegen et al., 2019) and GISS-E2.1-MATRIX (Fanourgakis et al., 2019).

Mode (abbreviation)	α_k	$\overline{r}\,(\mu\mathrm{m})$	$\rho\,(\mathrm{kg\,m^{-3}})$	κ
Dust (du)	$\alpha_{\mathrm{dust}} = 1$	0.93	2650	0.140
Sea salt (ss)	$\alpha_{\mathrm{sea\,salt}} = 1$	0.60	2165	1.335
Carbonaceous (ca)	$\alpha_{\mathrm{sulfate}} = 0.0839,\ \alpha_{\mathrm{organic\,carbon}} = 0.8745,\ \alpha_{\mathrm{black\,carbon}} = 0.0416$	0.16	1987	0.166
Sulfuric (su)	$\alpha_{\mathrm{sulfate}} = 0.8926,\ \alpha_{\mathrm{organic\,carbon}} = 0.0826,\ \alpha_{\mathrm{black\,carbon}} = 0.0248$	0.22	1858	0.464

3 Simulation setup

We performed a global simulation with ICON-MPIM together with HAM-lite at a resolution of five kilometers and over a period of one year. The simulation was configured as the cycle 3 simulation of nextGEMS (Koldunov et al., 2023). The sea surface temperature and sea ice were prescribed instead of simulating an interactive ocean and the inhomogeneity factor for liquid clouds was adjusted to tune the radiation balance at the top of atmosphere. The aerosols of HAM-lite were represented by four modes composed of dust, sea salt, organic carbon, black carbon, and sulfate.

3.1 Model configuration

Horizontally, the atmosphere and land are discretized with the R2B9 grid, which corresponds to a grid spacing of about five kilometers. Vertically, the atmosphere is divided into 90 levels with a thickness of $25 - 400\,\mathrm{m}$, and the land is divided into five levels with a thickness of $0.065 - 5700\,\mathrm{m}$. The time step of the atmosphere and land is $\Delta t_{\mathrm{A,L}} = 40\,\mathrm{s}$ and the time step of the radiation is $\Delta t_{\mathrm{rad}} = 12\,\mathrm{min}$. The initial conditions of the atmosphere and land were derived from the ERA5 reanalysis of the European Centre for Medium-Range Weather Forecasts (Hersbach et al., 2020). The boundary conditions for the ocean surface were taken from the AMIP II database (Taylor et al., 2000). The inhomogeneity factor for liquid clouds was increased from 0.4 to 0.8 in order to match the radiation balance at the top of atmosphere with observations (Mauritsen et al., 2022). The simulation started on 20 January 2020 at 00:00 UTC and ran until 1 February 2021.

The aerosols are represented with four modes as summarized in table 2. There are two pure modes, one of dust and one of sea salt, and two internally mixed modes, both of organic carbon, black carbon, and sulfate. The first mixed mode is dominated by carbon. It includes aerosols from forest fires, grass fires, agricultural waste burning, and biogenic emissions. The second mixed mode is dominated by sulfur. It includes aerosols from aviation, energy production and distribution, industry, maritime transport, land transport, waste treatment and disposal, residential and commercial combustion, and volcanoes. The emissions of the two mixed modes were taken from the AeroCom-II ACCMIP database following the RCP4.5 scenario (Heil et al., 2022). The densities and hygroscopicities of the species were taken from from ECHAM6.3-HAM2.3 (Tegen et al., 2019) and GISS-E2.1-MATRIX (Fanourgakis et al., 2019). The radii of the modes were initially taken from the MACv2 aerosol climatology of

Table 3. Wall-clock times of one day with HAM-lite ($\Delta t_{\text{wall,lite}}$) and without HAM-lite ($\Delta t_{\text{wall}}$) at two different resolutions (R2B4 and R2B9). Due to fluctuations, the wall-clock times were averaged over three independent simulations. Input/Output operations are not included. HAM-lite operations are given in brackets.

	$\Delta t_{\text{wall,lite}}$ (s)	Δt_{wall} (s)
R2B4		
Total integration	151.4	131.1
Parameterization schemes	109.9	84.7
Cloud microphysics	1.9 (1.0)	0.7
Radiation	35.0 (5.7)	27.7
Turbulence	59.3 (6.9)	52.5
Sedimentation	0.1 (0.1)	
R2B9		
Total integration	2016.7	933.0
Parameterization schemes	1230.2	409.8
Cloud microphysics	58.3 (32.2)	23.1
Radiation	199.0 (28.6)	155.3
Turbulence	448.6 (274.9)	149.8
Sedimentation	4.3 (4.3)	

Kinne (2019) and then adjusted to roughly match the aerosol lifetimes reported in Gliß et al. (2021). The simulation started from a clean atmosphere without aerosols.

3.2 Computational procedure

The simulation was performed and analyzed on the Levante cluster of the Deutsches Klimarechentrum GmbH (2024). The computational throughput was about 40 simulated days per day of wall-clock time on 400 compute nodes, each with 128 cores and 256 gigabyte memory. A significant amount of the simulation time was related to input/output operations. One variable at one level and one time step requires about 0.08 gigabytes of disk space. In summary, we stored about 250 terabytes including some fields in three dimensions or at high frequency to track and analyze various processes.

To assess the computational costs related to HAM-lite, we performed test runs with and without interactive aerosols at two different resolution, i.e., the coarse R2B4 grid on 2 nodes and the fine R2B9 grid on 400 nodes. Table 3 summarizes the wall-clock times of one simulated day without aerosols and with aerosols. It shows the total integration time but also a breakdown into parameterization schemes introduced in sections 2.2 and 2.3. Input/Output operations such as reading of boundary conditions are not included. The simulation with aerosols was about 1.2 times slower on the R2B4 grid and about 2.2 times slower on the R2B9 grid. The operations of HAM-lite took a relatively small amount of time. The majority of the additional time was related to operations outside of HAM-lite such as tracer transport. There are 10 atmospheric tracers without

Table 4. Global mean aerosol burdens and fluxes of ICON-HAM-lite averaged over February 2020 to January 2021.

	Burden (Tg)	Emission (Tg yr^{-1})	Dry depos. (Tg yr^{-1})	Wet depos. (Tg yr^{-1})
Dust	19.65	1873	1066	807.1
Sea salt	8.771	2823	369.3	2447
Carbonaceous	0.747	48.05	11.30	36.38
Sulfuric	2.817	219.2	42.90	175.5

aerosols compared to 14 atmospheric tracers with aerosols. And in contrast to the tracers of the cloud microphysics, the tracers
230 of the aerosols are computed on all levels throughout the atmospheric column.

4 Results and Discussion

Here, we present an initial analysis of the simulation outlined in section 3. In the first part, we analyze the global aerosol cycle
including burdens, lifetimes, fluxes, and optical depths. In the second part, we provide insights into regional processes such as
the formation of dust storms by thunderstorm outflows or the interplay of sea salt and tropical cyclones.

235 ### 4.1 Global cycle

To start with, we evaluate the global cycle of aerosols averaged over one year from February 2020 to January 2021. Due to
the large computational costs, we discard only the first 12 days from 20 January 2020 to 1 February 2020 as spin-up time.
Table 4 shows the aerosol burdens and fluxes of our simulation and table 5 shows the aerosol burdens, emissions, lifetimes,
and optical depths at $550\,\mathrm{nm}$ of our simulation and of the two model intercomparisons AeroCom phase 1 (Textor et al., 2006)
240 and phase 3 (Gliß et al., 2021). Note that our lifetimes were estimated by dividing burdens with emission fluxes (Seinfeld
and Pandis, 2016). And that our lifetimes are sensitive to the prescribed aerosol sizes listed in table 2. In general, the size
and lifetime of an aerosol are inversely related, i.e., a larger aerosol is activated and deposited more quickly than a smaller
aerosol. Despite the simplicity of our model, our values are comparable to those of AeroCom. To put into context, the values
of AeroCom, comparing more than 10 models, are subject to large uncertainties. For example, the standard deviations of the
245 lifetimes range between $29\,\%$ for organic aerosol to $91\,\%$ for sea salt. The largest differences between our simulation and
AeroCom are observed for carbonaceous aerosols, which is caused by too low biomass burning emissions (Tegen et al., 2019;
Salzmann et al., 2022). In future simulations, we plan to use emissions from the GFAS database (Kaiser et al., 2012).

To examine the distribution across the globe, figure 3 shows global maps of aerosol burdens averaged over one year. As
expected, the column burden of dust is large over the deserts in North Africa, Middle East, and East Asia. The column burden
250 of sea salt is governed by the interplay of storm tracks and rain bands over the ocean. Sea salt aerosols are quickly washed
out by marine clouds, and consequently their lifetime is about one day as show in table 5. The column burdens of the two
mixed modes are governed by the emission scenario. Carbonaceous aerosols are concentrated over biomass burning regions,

Table 5. Global mean aerosol burdens, emissions, lifetimes, and optical depths at $550\,\mathrm{nm}$ of ICON-HAM-lite averaged over February 2020 to January 2021 and the multi-model intercomparisons AeroCom phase 1 (Textor et al., 2006) and phase 3 (Gliß et al., 2021).

	Burden (Tg)	Emission ($\mathrm{Tg\,yr^{-1}}$)	Lifetime (d)	Optical depth
ICON-HAM-lite				
Dust	19.65	1873	3.828	0.0098
Sea salt	8.771	2823	1.133	0.0397
Carbonaceous	0.747	48.05	5.670	0.0074
Sulfuric	2.817	219.2	4.689	0.0347
AeroCom phase 1 (median)				
Dust	20.5	1640	4.0	0.032
Sea salt	6.4	6280	0.41	0.030
Black carbon	0.210	11.3	6.5	0.004
Organic aerosol	1.76	96.0	6.2	0.018
Sulfur	1.98	186.0	4.1	0.034
AeroCom phase 3 (median)				
Dust	16.6	1440	3.7	0.021
Sea salt	8.7	4980	0.56	0.044
Black carbon	0.131	9.7	5.5	0.002
Organic aerosol	1.91	116.0	6.0	0.022
Sulfur	1.80	143.0	4.9	0.035

primarily in Central Africa and East Asia. Whereas sulfuric aerosols are concentrated over industrial regions, for example in China and India. To better understand emission and deposition, figure 4 shows global maps of the dust burden and fluxes. Dust

255   aerosols are emitted by winds over the Sahara and Gobi desert. A large fraction of dust is deposited close to its source due its large radius and density given in table 2. A smaller fraction is transported over longer distances, for example, from the Sahara over the Atlantic and towards the Amazon.

    To examine the distribution throughout the column, figure 5 shows global mean vertical profiles of aerosol mixing ratios averaged over one year. Dust aerosols are lifted up to about $500\,\mathrm{hPa}$ by convective storms, and some dust aerosols rise even

260   further up to about $200\,\mathrm{hPa}$. In contrast, sea salt aerosols are washed out by low marine clouds, and only few sea salt aerosols rise above $800\,\mathrm{hPa}$. The profile of carbonaceous aerosols shows a local peak at about $150\,\mathrm{hPa}$, whereas the profile of sulfuric aerosols decreases monotonically with the pressure. Carbonaceous aerosols have a smaller number median radius and hygroscopicity than sulfuric aerosols as summarized in table 2. And consequently, carbonaceous aerosols are activated and deposited less effectively. Note that the vertical distribution of aerosols is weakly constrained by observations and highly variable among
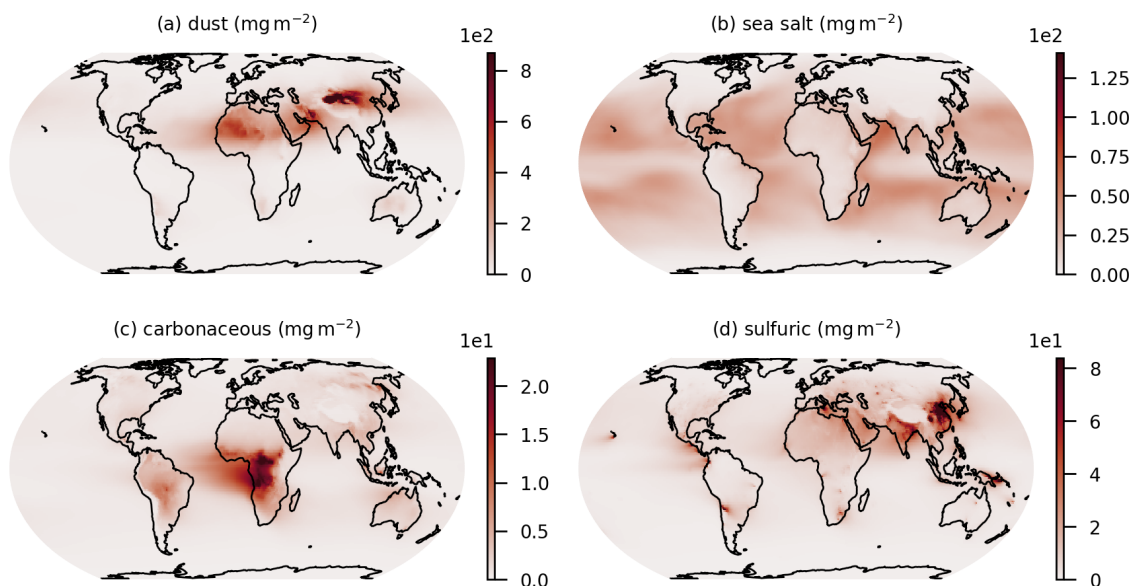
Figure 3. Column burdens of aerosols averaged over February 2020 to January 2021: dust (a), sea salt (b), carbonaceous aerosol (c), and sulfuric aerosol (d).

265   AeroCom models (Kipling et al., 2016; Koffi et al., 2016). And besides convective transport, microphysical and chemical processes such as condensation or coagulation play an important role (Watson-Parris et al., 2019).

    Finally, we evaluate the aerosol optical depth at $550\,\mathrm{nm}$. Figure 6 shows optical depths of our simulation and the MODIS-Aqua satellite (Platnick et al., 2015). The optical depth of our simulation was averaged over one year, whereas the optical depth of MODIS-Aqua was averaged over five years from 2018 to 2022. Note that observations from satellites are subject to some 270 uncertainties as discussed by Vogel et al. (2022). Within $60°\,\mathrm{S}$ to $60°\,\mathrm{N}$, the average optical depth of our simulation (0.104) is lower than that of MODIS-Aqua (0.168). Table 5 reveals that this bias is mainly related to the optical depths of carbonaceous and dust aerosols. There are several ways to address this bias. First, we plan to revise the biomass burning emissions. As already mentioned, previous studies showed that those emissions are too low compared to observations (Kaiser et al., 2012; Tegen et al., 2019; Salzmann et al., 2022) Second, we plan to fine tune the aerosol properties listed in table 2. As already 275 mentioned, the aerosol sizes have large impacts on the lifetimes and optical depths. In addition, one could revise the removal processes, for example, the resistances in the dry deposition scheme or the activation fraction in the wet deposition scheme.

4.2 Regional insights

After the global overview, we provide insights into regional processes that are only resolved in kilometer-scale simulations. Figure 7 shows a scene of aerosols and clouds on 10 August 2020 at 00:00 UTC. It shows the horizontal distribution of aerosol 280 burdens as well as the vertical distribution of aerosols and cloud water and ice along the prime meridian. In order to show all
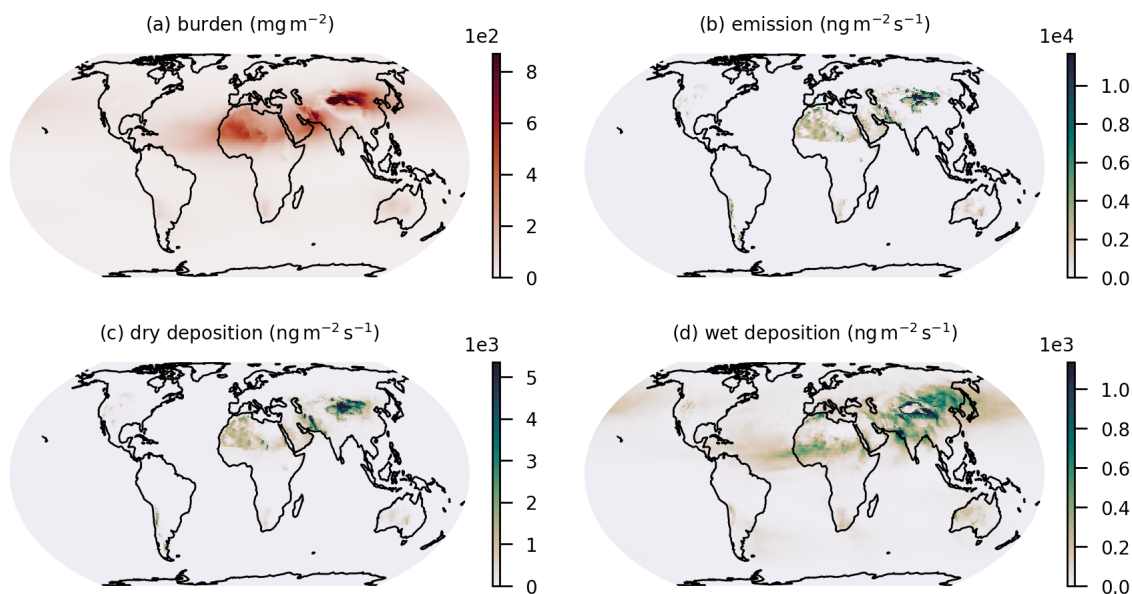
Figure 4. Column burden and fluxes of dust averaged over February 2020 to January 2021: burden (a), emission (b), dry deposition (c), and wet deposition (d).
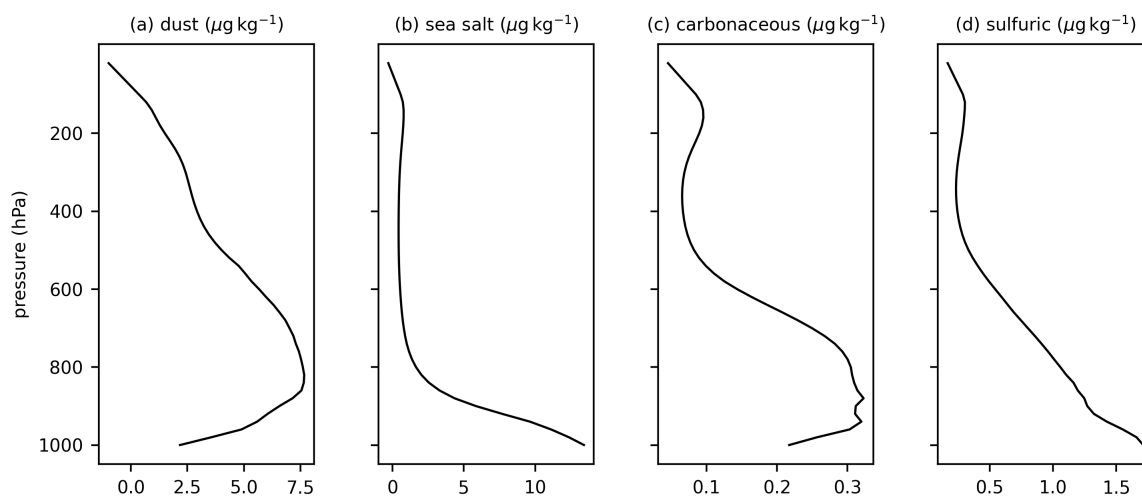
Figure 5. Global mean mass mixing ratios of aerosols averaged over February 2020 to January 2021: dust (a), sea salt (b), carbonaceous aerosol (c), and sulfuric aerosol (d).

modes in one frame, the colormaps have a variable transparency. The images capture various processes in a new level of detail. Dust aerosols are lifted above $400\,\mathrm{hPa}$ by convective storms over the Sahara. Sea salt aerosols are washed out by low marine
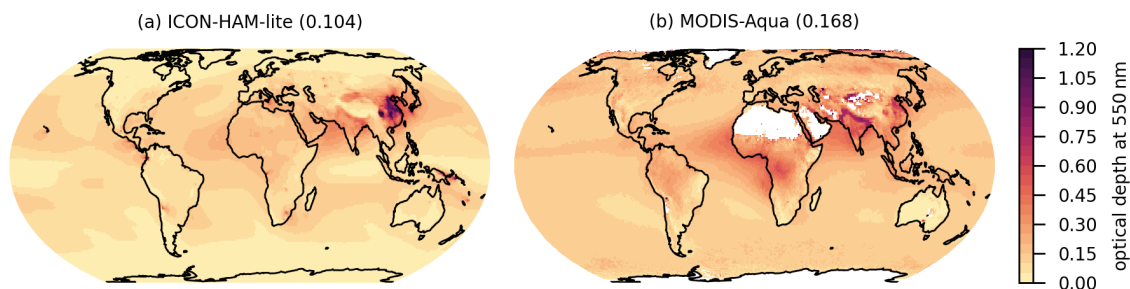
Figure 6. Aerosol optical depth at $550\,\text{nm}$ from this simulation averaged over February 2020 to January 2021 (a) and from MODIS-Aqua (Platnick et al., 2015) averaged over 2018 to 2022 (b). The spatial average over $60°\,\text{S}$ to $60°\,\text{N}$ is given in brackets.

clouds below $800\,\text{hPa}$. Carbonaceous aerosols are emitted by forest fires in Central Africa and blown over the Atlantic by trade winds. And sulfuric aerosols are emitted by anthropogenic and volcanic activity and lifted up to $200\,\text{hPa}$.

285   To highlight the interaction of aerosols and clouds, figure 8 shows a scene of sea salt aerosols, cloud water and ice, and precipitation on 4 September 2020 at 00:00 UTC. It provides a global overview and highlights a tropical cyclone in the Atlantic and a weather front in the Indian Ocean. Like in figure 7, the colormaps have a variable transparency. The global overview shows how sea salt aerosols are emitted by surface winds and deposited by rain bands. The distribution of sea salt aerosols is rather variable due to their short lifetimes of about one day. Low burdens can be seen, for example, in the Pacific or Southern

290 Ocean, whereas high burdens can be seen in the Atlantic or Indian Ocean. The tropical cyclone is associated with large wind speeds, precipitation rates, and sea salt burdens. Previous studies suggest that aerosols can modulate the intensity of cyclones. Although these results were subject to model details such as the representation of cloud microphysics (Khain et al., 2016; Hoarau et al., 2018).

    To highlight the interaction of convective storms and dust emissions, figure 9 shows a scene of dust aerosols over the Sahara

295 on 23 July 2020 at 21:00 UTC. It shows the mass mixing ratios of dust at the lowest model level and the vertical velocities at $850\,\text{hPa}$. The vertical velocities highlight diverging cold pool edges that lift air from convective downdrafts. These cold pool outflows drive intense dust storms, also known as haboobs, that move towards the western coast. Haboobs generate a large fraction of the global dust burden and impact the global energy budget of Earth (Kok et al., 2023). Coarse-resolution models without resolved convection cannot capture the dynamics of cold pools and associated dust storms and need to compensate for

300 that with tuning parameters (Marsham et al., 2011). This highlights the strong potential of kilometer-scale models to adequately represent small-scale processes that drive the global dust cycle (Heinold et al., 2013; Senior et al., 2021).

    To highlight the interaction of surface winds and sea salt emissions, figure 10 shows a scene of sea salt aerosols over the Atlantic on 13 December 2020 at 00:00 UTC. It shows the mass mixing ratios of sea salt in the lowest model level and the the wind speeds at 10 meters above the surface. There are various small and large-scale features. The large area of high sea salt

305 concentrations is related to persistent trade winds. The large band of low sea salt concentrations across the Atlantic reflects a large zone of calm winds, also known as doldrums. Despite its large extend, this zone is not captured accurately in coarse-
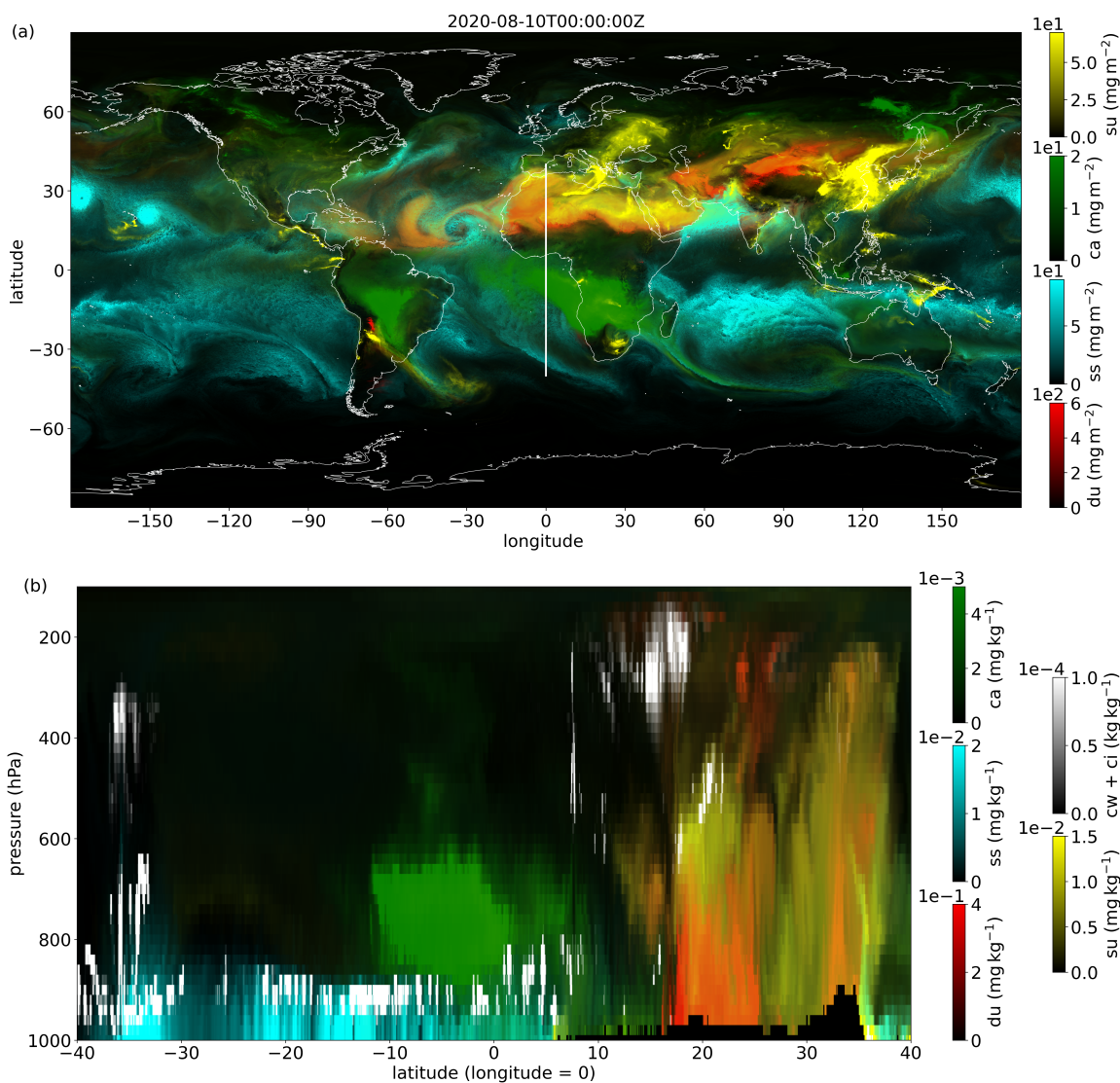
Figure 7. Scene of aerosols and clouds on 10 August 2020 at 00:00 UTC. Figure (a) shows column burdens of dust (du) in red, sea salt (ss) in blue, carbonaceous aerosol (ca) in green, and sulfuric aerosol (su) in yellow. Figure (b) shows the corresponding mass mixing ratios together with the mass mixing ratio of cloud water and ice (cw + ci) in white along the prime meridian indicated in figure (a). The colormaps have a variable transparency which decreases from fully transparent at minima to fully opaque at maxima.

resolution simulations. And lastly, the small circular features were caused by shallow convective storms or deep convective clusters associated with intense precipitation (Klocke et al., 2017).
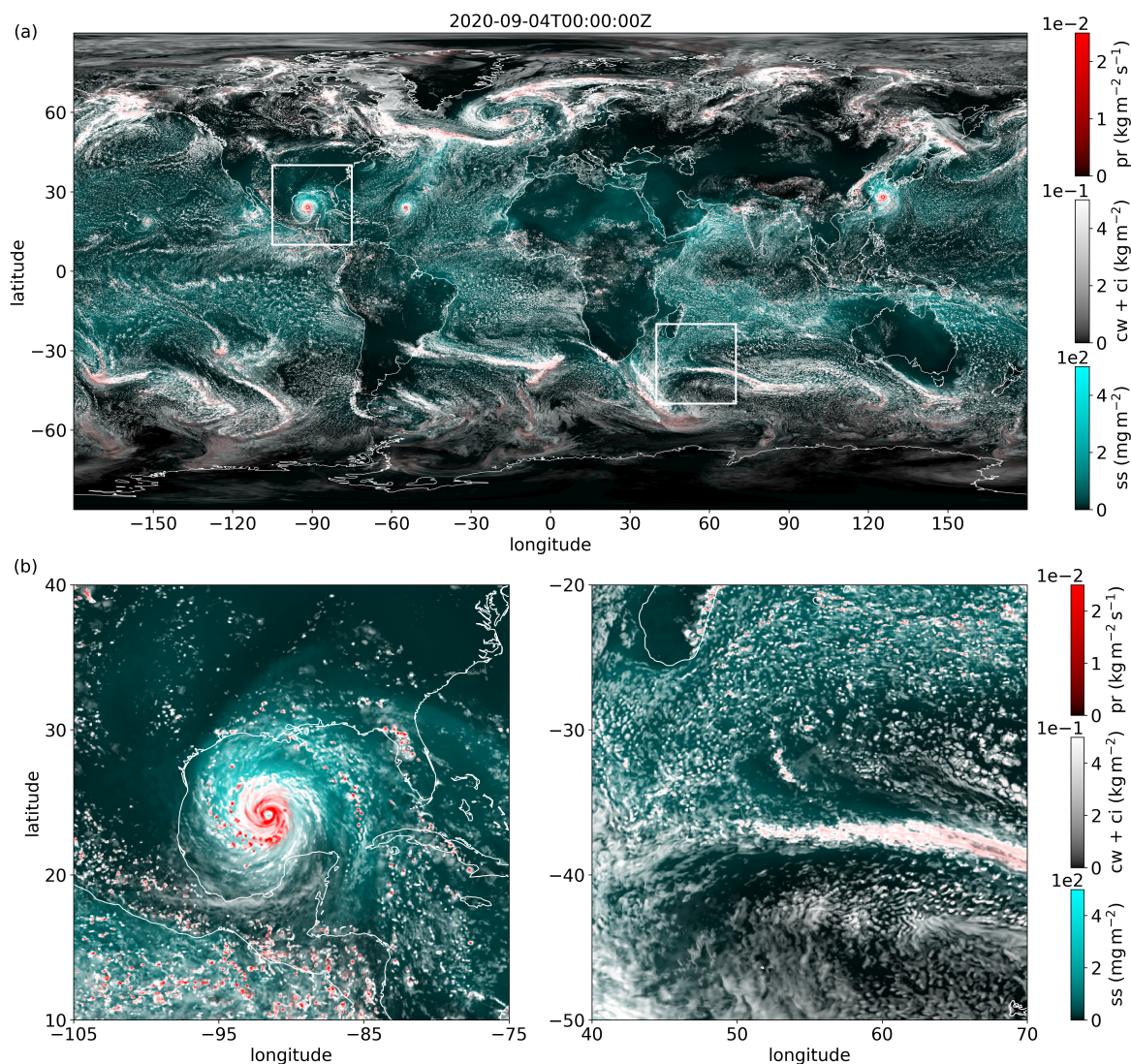
Figure 8. Scene of sea salt, cloud water and ice, and precipitation on 4 September 2020 at 00:00 UTC. Figure (a) shows column burden of sea salt (ss) in blue, column burden of cloud water and ice (cw + ci) in white, and surface precipitation (pr) in red. Insets (b) show a tropical cyclone in the Gulf of Mexico and a weather front in the Indian Ocean. The colormaps have a variable transparency which decreases from fully transparent at minima to fully opaque at maxima.

5 Conclusion and Outlook

310   We introduced a new one-moment aerosol module HAM-lite that is traceable to the two-moment module HAM (Stier et al., 2005; Salzmann et al., 2022). Aerosols are represented as an ensemble of log-normal modes with prescribed mean radius and standard deviation. The modal structure of HAM-lite is flexible. The size and composition of modes can be chosen according
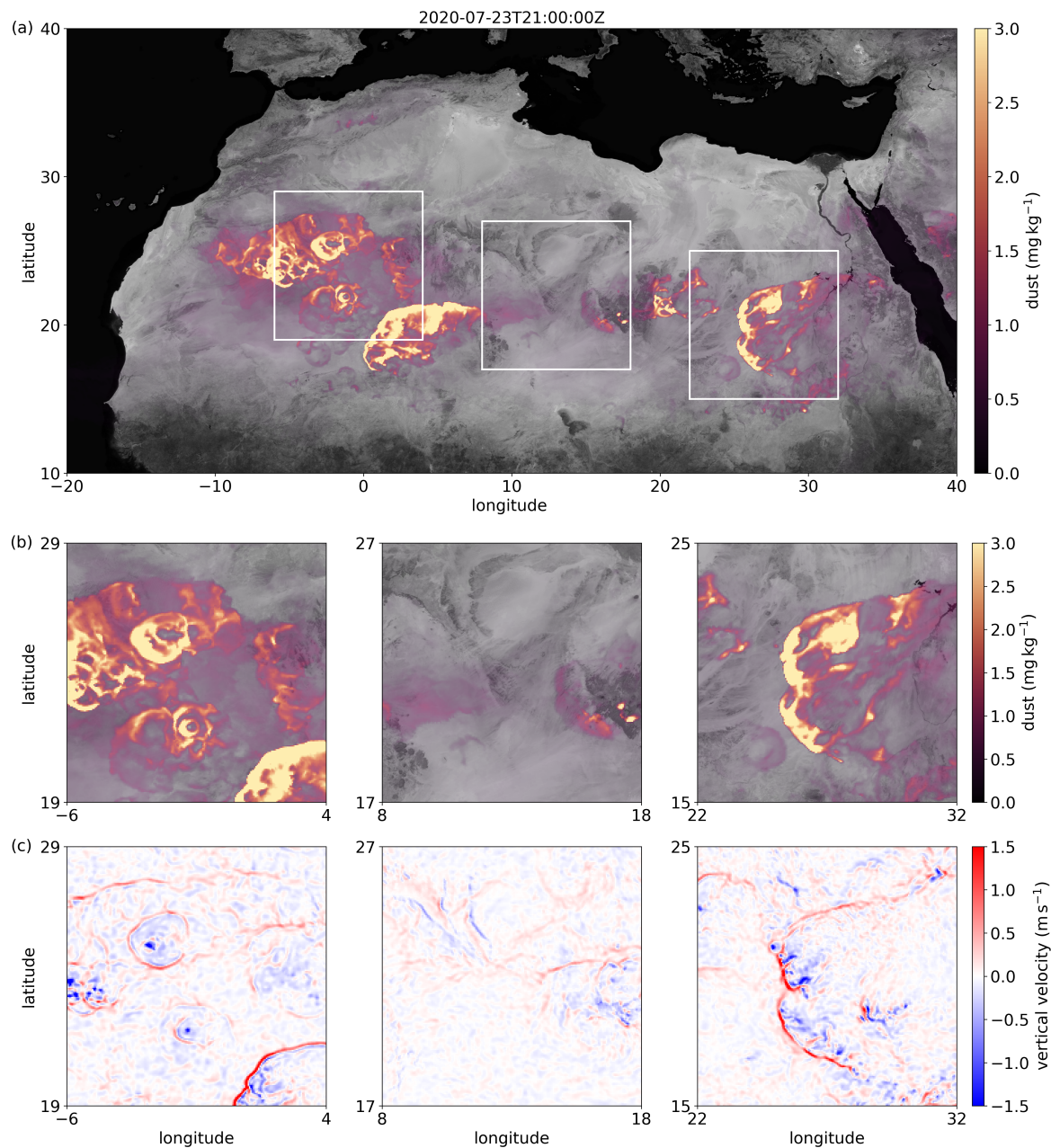
Figure 9. Scene of dust over the Sahara on 23 July 2020 at 21:00 UTC. Figure (a) and insets (b) show mass mixing ratio of dust at the lowest model level above the surface. Insets (c) show vertical velocity at $850\,\mathrm{hPa}$. The colormaps of figure (a) and insets (b) have a variable transparency which decreases from fully transparent at minima to fully opaque at maxima. The background is the Blue Marble composite of NASA Earth Observatory (2024) converted to grayscale.
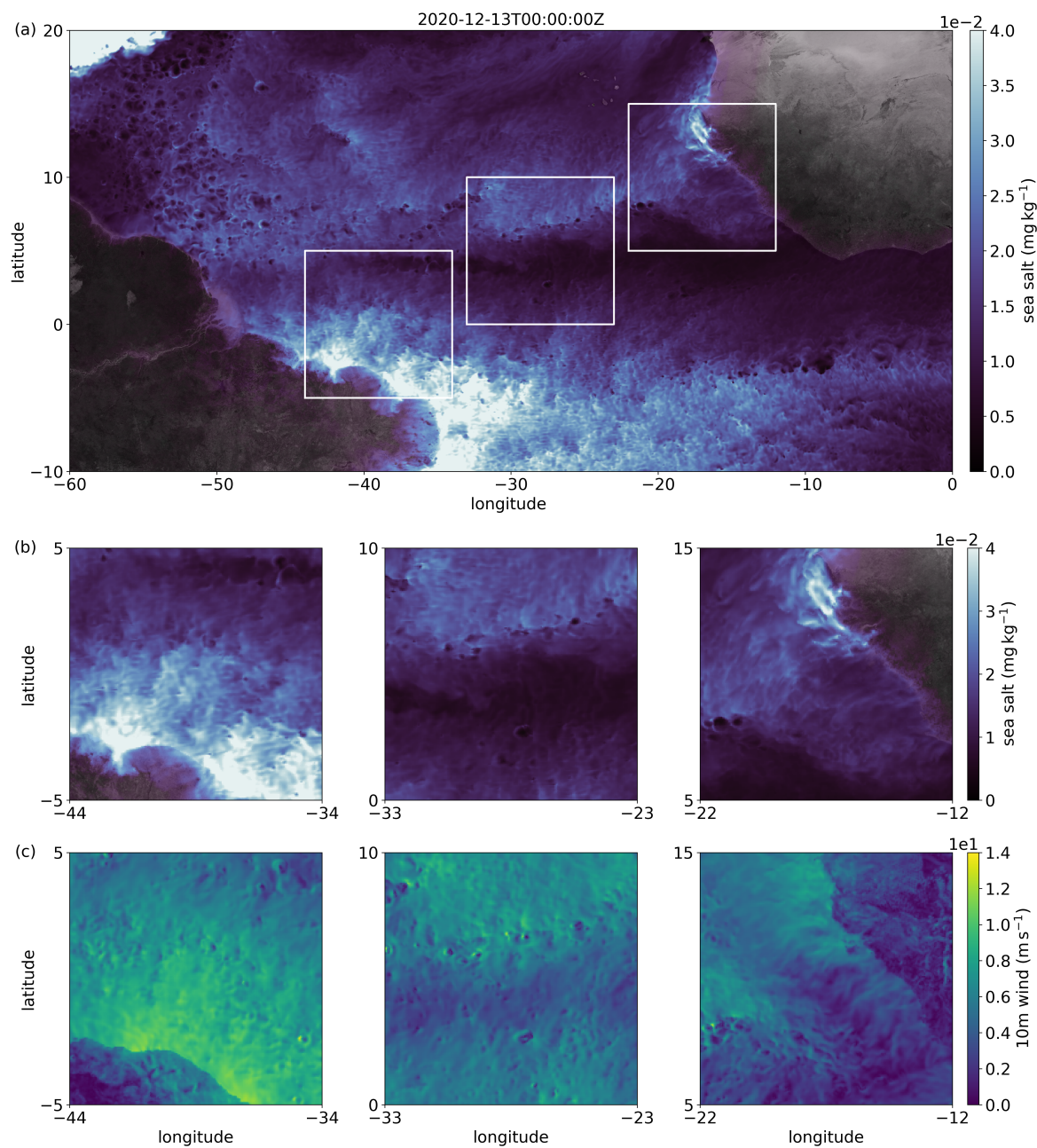
Figure 10. Scene of sea salt over the Atlantic on 13 December 2020 at 00:00 UTC. Figure (a) and insets (b) show mass mixing ratio of sea salt at the lowest model level above the surface. Insets (c) show wind speed at 10 meter above surface. The colormaps of figure (a) and insets (b) have a variable transparency which decreases from fully transparent at minima to fully opaque at maxima. The background is the Blue Marble composite of NASA Earth Observatory (2024) converted to grayscale.

to the computational resources and research question. To test our module, we performed a year-long simulation with four idealized aerosol modes. There were two pure modes, one of dust and one of sea salt, and two internally mixed modes, both of organic carbon, black carbon, and sulfate. The atmosphere and land were resolved with a resolution of five kilometers, and the sea surface temperature and sea ice were prescribed.

We presented an overview of the global aerosol cycle and provided insights into regional aerosol processes that are only resolved at kilometer scales. The global overview showed that the aerosol lifetimes are comparable to those reported in previous model intercomparisons (Textor et al., 2006; Gliß et al., 2021). The aerosol optical depth is, however, lower than expected, also in comparison with satellite observations (Vogel et al., 2022). To address this bias, we plan to update the biomass burning emissions and to revise the prescribed aerosol properties. The regional insights captured key aerosol processes at a new level of detail. Dust aerosols are lifted up by cold pool outflows in the Sahara and transported towards the Amazon. Sea salt aerosols are washed out by low marine clouds and interact with tropical cyclones. Carbonaceous aerosols are emitted from wild and forest fires and blown over the Atlantic by trade winds. Sulfuric aerosols are emitted from anthropogenic activities and transported across the Northern hemisphere. These results demonstrate that kilometer-scale simulations with interactive aerosols are possible and that such simulations can provide new insights into the role of aerosols in the Earth system.

There are many plans and ideas for future research. Most importantly, we plan to evaluate the aerosol processes more in-depth, to update the emission database, and to fine tune parameters like aerosol size. On the model development side, we cooperate with other groups to implement a new dust emission scheme from Klose et al. (2021), to include emissions of dimethyl sulfide (Fung et al., 2022), and to couple the aerosol module with the two-moment cloud microphysics scheme from Seifert and Beheng (2006), which would allow us to examine aerosol-cloud interactions in more detail. And on the scientific side, we plan to perform simulations with pre-industrial and present-day emission scenarios in order to estimate the effective radiative forcing (Forster et al., 2021), to analyze dust storms and deep convective clouds in a Lagrangian manner (Jones et al., 2024), and to compare our simulations with the incoming observations from the EarthCARE mission (Wehr et al., 2023).

Code and data availability. The source code is available on the GitLab of the DKRZ (https://gitlab.dkrz.de/icon/icon-mpim) under a BSD 3-clause license (https://gitlab.dkrz.de/icon/icon-mpim/-/tree/master/LICENSES). The simulations were performed with the branch feature_hamlite at commit 06404746. Derived data in support of the findings presented above can be found on the Levante cluster of the DKRZ (https://www.dkrz.de/en/systems/hpc/hlre-4-levante). Users need to register at DKRZ to access GitLab and Levante (https://luv.dkrz.de/register/). To access the source code repository, users need to be granted access to the ICON development project (https://luv.dkrz.de/projects/1125/).

Author contributions. The aerosol module HAM-lite was developed by Philipp Weiss with support from Ross Herbert and Philip Stier. The simulations were performed by Philipp Weiss. The paper was drafted by Philipp Weiss and revised by Ross Herbert and Philip Stier. And the project was outlined and guided by Philip Stier.

Competing interests. The author declare no competing interests.

345   *Acknowledgements.* The simulations were performed and analyzed on the Levante cluster of the DKRZ with resources granted under project 1368 (https://www.dkrz.de/en/systems/hpc/hlre-4-levante). The authors acknowledge funding from the Horizon 2020 projects nextGEMS under grant agreement 101003470 and FORCeS under grant agreement 821205. Ross Herbert and Philip Stier acknowledge funding from the Horizon 2020 project RECAP under grant agreement 724602. And Philip Stier acknowledges funding from the Horizon Europe project CleanCloud under grant agreement 101137639 and its UKRI underwrite.

References

Abdul-Razzak, H. and Ghan, S. J.: A parameterization of aerosol activation: 2. Multiple aerosol types, Journal of Geophysical Research: Atmospheres, 105, 6837–6844, https://doi.org/10.1029/1999JD901161, 2000.

Baldauf, M., Seifert, A., Förstner, J., Majewski, D., Raschendorfer, M., and Reinhardt, T.: Operational Convective-Scale Numerical Weather Prediction with the COSMO Model: Description and Sensitivities, Monthly Weather Review, 139, 3887 – 3905, https://doi.org/10.1175/MWR-D-10-05013.1, 2011.

Bohren, C. F. and Huffman, D. R.: Absorption and Scattering of Light by Small Particles, John Wiley & Sons, Ltd, ISBN 9783527618156, https://doi.org/10.1002/9783527618156, 1998.

Boucher, O., Randall, D., Artaxo, P., Bretherton, C., Feingold, G., Forster, P., Kerminen, V.-M., Kondo, Y., Liao, H., Lohmann, U., Rasch, P., Satheesh, S., Sherwood, S., Stevens, B., and Zhang, X.: Clouds and Aerosols, in: Climate Change 2013: The Physical Science Basis. Contribution of Working Group I to the Fifth Assessment Report of the Intergovernmental Panel on Climate Change, edited by Stocker, T., Qin, D., Plattner, G.-K., Tignor, M., Allen, S., Boschung, J., Nauels, A., Xia, Y., Bex, V., and Midgley, P., Cambridge University Press, Cambridge, United Kingdom and New York, NY, USA, 2013.

Deutsches Klimarechentrum GmbH: Levante HPC System, https://www.dkrz.de/en/systems/hpc/hlre-4-levante, 2024.

Dipankar, A., Stevens, B., Heinze, R., Moseley, C., Zängl, G., Giorgetta, M., and Brdar, S.: Large eddy simulation using the general circulation model ICON, Journal of Advances in Modeling Earth Systems, 7, 963–986, https://doi.org/10.1002/2015MS000431, 2015.

Fanourgakis, G. S., Kanakidou, M., Nenes, A., Bauer, S. E., Bergman, T., Carslaw, K. S., Grini, A., Hamilton, D. S., Johnson, J. S., Karydis, V. A., Kirkevåg, A., Kodros, J. K., Lohmann, U., Luo, G., Makkonen, R., Matsui, H., Neubauer, D., Pierce, J. R., Schmale, J., Stier, P., Tsigaridis, K., van Noije, T., Wang, H., Watson-Parris, D., Westervelt, D. M., Yang, Y., Yoshioka, M., Daskalakis, N., Decesari, S., Gysel-Beer, M., Kalivitis, N., Liu, X., Mahowald, N. M., Myriokefalitakis, S., Schrödner, R., Sfakianaki, M., Tsimpidi, A. P., Wu, M., and Yu, F.: Evaluation of global simulations of aerosol particle and cloud condensation nuclei number, with implications for cloud droplet formation, Atmospheric Chemistry and Physics, 19, 8591–8617, https://doi.org/10.5194/acp-19-8591-2019, 2019.

Forster, P., Storelvmo, T., Armour, K., Collins, W., Dufresne, J.-L., Frame, D., Lunt, D., Mauritsen, T., Palmer, M., Watanabe, M., Wild, M., and Zhang, H.: The Earth's Energy Budget, Climate Feedbacks and Climate Sensitivity, in: Climate Change 2021: The Physical Science Basis. Contribution of Working Group I to the Sixth Assessment Report of the Intergovernmental Panel on Climate Change, edited by Masson-Delmotte, V., Zhai, P., Pirani, A., Connors, S., Péan, C., Berger, S., Caud, N., Chen, Y., Goldfarb, L., Gomis, M., Huang, M., Leitzell, K., Lonnoy, E., Matthews, J., Maycock, T., Waterfield, T., Yelekçi, O., Yu, R., and Zhou, B., pp. 923–1054, Cambridge University Press, Cambridge, United Kingdom and New York, https://doi.org/10.1017/9781009157896.009, 2021.

Fung, K. M., Heald, C. L., Kroll, J. H., Wang, S., Jo, D. S., Gettelman, A., Lu, Z., Liu, X., Zaveri, R. A., Apel, E. C., Blake, D. R., Jimenez, J.-L., Campuzano-Jost, P., Veres, P. R., Bates, T. S., Shilling, J. E., and Zawadowicz, M.: Exploring dimethyl sulfide (DMS) oxidation and implications for global aerosol radiative forcing, Atmospheric Chemistry and Physics, 22, 1549–1573, https://doi.org/10.5194/acp-22-1549-2022, 2022.

Giorgetta, M. A., Brokopf, R., Crueger, T., Esch, M., Fiedler, S., Helmert, J., Hohenegger, C., Kornblueh, L., Köhler, M., Manzini, E., Mauritsen, T., Nam, C., Raddatz, T., Rast, S., Reinert, D., Sakradzija, M., Schmidt, H., Schneck, R., Schnur, R., Silvers, L., Wan, H., Zängl, G., and Stevens, B.: ICON-A, the Atmosphere Component of the ICON Earth System Model: I. Model Description, Journal of Advances in Modeling Earth Systems, 10, 1613–1637, https://doi.org/10.1029/2017MS001242, 2018.

Gliß, J., Mortier, A., Schulz, M., Andrews, E., Balkanski, Y., Bauer, S. E., Benedictow, A. M. K., Bian, H., Checa-Garcia, R., Chin, M., Ginoux, P., Griesfeller, J. J., Heckel, A., Kipling, Z., Kirkevåg, A., Kokkola, H., Laj, P., Le Sager, P., Lund, M. T., Lund Myhre, C., Matsui, H., Myhre, G., Neubauer, D., van Noije, T., North, P., Olivié, D. J. L., Rémy, S., Sogacheva, L., Takemura, T., Tsigaridis, K., and Tsyro, S. G.: AeroCom phase III multi-model evaluation of the aerosol life cycle and optical properties using ground- and space-based remote sensing as well as surface in situ observations, Atmospheric Chemistry and Physics, 21, 87–128, https://doi.org/10.5194/acp-21-87-2021, 2021.

Gong, S. L.: A parameterization of sea-salt aerosol source function for sub- and super-micron particles, Global Biogeochemical Cycles, 17, https://doi.org/10.1029/2003GB002079, 2003.

Goto, D., Sato, Y., Yashiro, H., Suzuki, K., Oikawa, E., Kudo, R., Nagao, T. M., and Nakajima, T.: Global aerosol simulations using NICAM.16 on a 14 km grid spacing for a climate study: improved and remaining issues relative to a lower-resolution model, Geoscientific Model Development, 13, 3731–3768, https://doi.org/10.5194/gmd-13-3731-2020, 2020.

Heil, A., Schultz, M., and Granier, C.: AeroCom II emission data, https://aerocom-classic.met.no/DATA/download/emissions/AEROCOM-II-ACCMIP/, 2022.

Heinold, B., Knippertz, P., Marsham, J. H., Fiedler, S., Dixon, N. S., Schepanski, K., Laurent, B., and Tegen, I.: The role of deep convection and nocturnal low-level jets for dust emission in summertime West Africa: Estimates from convection-permitting simulations, Journal of Geophysical Research: Atmospheres, 118, 4385–4400, https://doi.org/10.1002/jgrd.50402, 2013.

Hersbach, H., Bell, B., Berrisford, P., Hirahara, S., Horányi, A., Muñoz-Sabater, J., Nicolas, J., Peubey, C., Radu, R., Schepers, D., Simmons, A., Soci, C., Abdalla, S., Abellan, X., Balsamo, G., Bechtold, P., Biavati, G., Bidlot, J., Bonavita, M., De Chiara, G., Dahlgren, P., Dee, D., Diamantakis, M., Dragani, R., Flemming, J., Forbes, R., Fuentes, M., Geer, A., Haimberger, L., Healy, S., Hogan, R. J., Hólm, E., Janisková, M., Keeley, S., Laloyaux, P., Lopez, P., Lupu, C., Radnoti, G., de Rosnay, P., Rozum, I., Vamborg, F., Villaume, S., and Thépaut, J.-N.: The ERA5 global reanalysis, Quarterly Journal of the Royal Meteorological Society, 146, 1999–2049, https://doi.org/10.1002/qj.3803, 2020.

Hinds, W. C. and Zhu, Y.: Aerosol Technology: Properties, Behavior, and Measurement of Airborne Particles, John Wiley & Sons, 1982.

Hoarau, T., Barthe, C., Tulet, P., Claeys, M., Pinty, J. P., Bousquet, O., Delanoë, J., and Vié, B.: Impact of the Generation and Activation of Sea Salt Aerosols on the Evolution of Tropical Cyclone Dumile, Journal of Geophysical Research: Atmospheres, 123, 8813–8831, https://doi.org/10.1029/2017JD028125, 2018.

Hohenegger, C., Korn, P., Linardakis, L., Redler, R., Schnur, R., Adamidis, P., Bao, J., Bastin, S., Behravesh, M., Bergemann, M., Biercamp, J., Bockelmann, H., Brokopf, R., Brüggemann, N., Casaroli, L., Chegini, F., Datseris, G., Esch, M., George, G., Giorgetta, M., Gutjahr, O., Haak, H., Hanke, M., Ilyina, T., Jahns, T., Jungclaus, J., Kern, M., Klocke, D., Kluft, L., Kölling, T., Kornblueh, L., Kosukhin, S., Kroll, C., Lee, J., Mauritsen, T., Mehlmann, C., Mieslinger, T., Naumann, A. K., Paccini, L., Peinado, A., Praturi, D. S., Putrasahan, D., Rast, S., Riddick, T., Roeber, N., Schmidt, H., Schulzweida, U., Schütte, F., Segura, H., Shevchenko, R., Singh, V., Specht, M., Stephan, C. C., von Storch, J.-S., Vogel, R., Wengel, C., Winkler, M., Ziemen, F., Marotzke, J., and Stevens, B.: ICON-Sapphire: simulating the components of the Earth system and their interactions at kilometer and subkilometer scales, Geoscientific Model Development, 16, 779–811, https://doi.org/10.5194/gmd-16-779-2023, 2023.

Jones, W. K., Stengel, M., and Stier, P.: A Lagrangian perspective on the lifecycle and cloud radiative effect of deep convective clouds over Africa, Atmospheric Chemistry and Physics, 24, 5165–5180, https://doi.org/10.5194/acp-24-5165-2024, 2024.

Kaiser, J. W., Heil, A., Andreae, M. O., Benedetti, A., Chubarova, N., Jones, L., Morcrette, J.-J., Razinger, M., Schultz, M. G., Suttie, M., and van der Werf, G. R.: Biomass burning emissions estimated with a global fire assimilation system based on observed fire radiative power, Biogeosciences, 9, 527–554, https://doi.org/10.5194/bg-9-527-2012, 2012.

425 Khain, A., Lynn, B., and Shpund, J.: High resolution WRF simulations of Hurricane Irene: Sensitivity to aerosols and choice of microphysical schemes, Atmospheric Research, 167, 129–145, https://doi.org/10.1016/j.atmosres.2015.07.014, 2016.

Kinne, S.: The MACv2 aerosol climatology, Tellus B: Chemical and Physical Meteorology, 71, 1–21, https://doi.org/10.1080/16000889.2019.1623639, 2019.

Kipling, Z., Stier, P., Johnson, C. E., Mann, G. W., Bellouin, N., Bauer, S. E., Bergman, T., Chin, M., Diehl, T., Ghan, S. J., Iversen,
430 T., Kirkevåg, A., Kokkola, H., Liu, X., Luo, G., van Noije, T., Pringle, K. J., von Salzen, K., Schulz, M., Seland, Ø., Skeie, R. B., Takemura, T., Tsigaridis, K., and Zhang, K.: What controls the vertical distribution of aerosol? Relationships between process sensitivity in HadGEM3–UKCA and inter-model variation from AeroCom Phase II, Atmospheric Chemistry and Physics, 16, 2221–2241, https://doi.org/10.5194/acp-16-2221-2016, 2016.

Klocke, D., Brueck, M., Hohenegger, C., and Stevens, B.: Rediscovery of the doldrums in storm-resolving simulations over the tropical
435 Atlantic, Nature Geoscience, 10, 891–896, https://doi.org/10.1038/s41561-017-0005-4, 2017.

Klose, M., Jorba, O., Gonçalves Ageitos, M., Escribano, J., Dawson, M. L., Obiso, V., Di Tomaso, E., Basart, S., Montané Pinto, G., Macchia, F., Ginoux, P., Guerschman, J., Prigent, C., Huang, Y., Kok, J. F., Miller, R. L., and Pérez García-Pando, C.: Mineral dust cycle in the Multiscale Online Nonhydrostatic AtmospheRe CHemistry model (MONARCH) Version 2.0, Geoscientific Model Development, 14, 6403–6444, https://doi.org/10.5194/gmd-14-6403-2021, 2021.

440 Koffi, B., Schulz, M., Bréon, F.-M., Dentener, F., Steensen, B. M., Griesfeller, J., Winker, D., Balkanski, Y., Bauer, S. E., Bellouin, N., Berntsen, T., Bian, H., Chin, M., Diehl, T., Easter, R., Ghan, S., Hauglustaine, D. A., Iversen, T., Kirkevåg, A., Liu, X., Lohmann, U., Myhre, G., Rasch, P., Seland, Ø., Skeie, R. B., Steenrod, S. D., Stier, P., Tackett, J., Takemura, T., Tsigaridis, K., Vuolo, M. R., Yoon, J., and Zhang, K.: Evaluation of the aerosol vertical distribution in global aerosol models through comparison against CALIOP measurements: AeroCom phase II results, Journal of Geophysical Research: Atmospheres, 121, 7254–7283, https://doi.org/10.1002/2015JD024639, 2016.

445 Kok, J. F., Storelvmo, T., Karydis, V. A., Adebiyi, A. A., Mahowald, N. M., Evan, A. T., He, C., and Leung, D. M.: Mineral dust aerosol impacts on global climate and climate change, Nature Reviews Earth & Environment, 4, 71–86, https://doi.org/10.1038/s43017-022-00379-5, 2023.

Koldunov, N., Kölling, T., Pedruzo-Bagazgoitia, X., Rackow, T., Redler, R., Sidorenko, D., Wieners, K.-H., and Ziemen, F. A.: nextGEMS: output of the model development cycle 3 simulations for ICON and IFS, https://doi.org/10.26050/WDCC/nextGEMS_cyc3, 2023.

450 Malavelle, F. F., Haywood, J. M., Field, P. R., Hill, A. A., Abel, S. J., Lock, A. P., Shipway, B. J., and McBeath, K.: A method to represent subgrid-scale updraft velocity in kilometer-scale models: Implication for aerosol activation, Journal of Geophysical Research: Atmospheres, 119, 4149–4173, https://doi.org/10.1002/2013JD021218, 2014.

Marsham, J. H., Knippertz, P., Dixon, N. S., Parker, D. J., and Lister, G. M. S.: The importance of the representation of deep convection for modeled dust-generating winds over West Africa during summer, Geophysical Research Letters, 38,
455 https://doi.org/10.1029/2011GL048368, 2011.

Mauritsen, T., Redler, R., Esch, M., Stevens, B., Hohenegger, C., Klocke, D., Brokopf, R., Haak, H., Linardakis, L., Röber, N., and Schnur, R.: Early Development and Tuning of a Global Coupled Cloud Resolving Model, and its Fast Response to Increasing CO2, Tellus A: Dynamic Meteorology and Oceanography, https://doi.org/10.16993/tellusa.54, 2022.

NASA Earth Observatory: Blue Marble Next Generation, https://visibleearth.nasa.gov/collection/1484/blue-marble, 2024.

Petters, M. D. and Kreidenweis, S. M.: A single parameter representation of hygroscopic growth and cloud condensation nucleus activity, Atmospheric Chemistry and Physics, 7, 1961–1971, https://doi.org/10.5194/acp-7-1961-2007, 2007.

Pincus, R., Mlawer, E. J., and Delamere, J. S.: Balancing Accuracy, Efficiency, and Flexibility in Radiation Calculations for Dynamical Models, Journal of Advances in Modeling Earth Systems, 11, 3074–3089, https://doi.org/10.1029/2019MS001621, 2019.

Platnick, S., Hubanks, P., Meyer, K., and King, M. D.: MODIS Atmosphere L3 Monthly Product (08_L3), https://modis.gsfc.nasa.gov/data/dataprod/mod08.php, 2015.

Pleim, J. E., Ran, L., Saylor, R. D., Willison, J., and Binkowski, F. S.: A New Aerosol Dry Deposition Model for Air Quality and Climate Modeling, Journal of Advances in Modeling Earth Systems, 14, e2022MS003 050, https://doi.org/10.1029/2022MS003050, e2022MS003050 2022MS003050, 2022.

Prein, A. F., Langhans, W., Fosser, G., Ferrone, A., Ban, N., Goergen, K., Keller, M., Tölle, M., Gutjahr, O., Feser, F., Brisson, E., Kollet, S., Schmidli, J., van Lipzig, N. P. M., and Leung, R.: A review on regional convection-permitting climate modeling: Demonstrations, prospects, and challenges, Reviews of Geophysics, 53, 323–361, https://doi.org/10.1002/2014RG000475, 2015.

Reick, C. H., Gayler, V., Goll, D., Hagemann, S., Heidkamp, M., Nabel, J., Raddatz, T., Roeckner, E., Schnur, R., and Wilkenskjeld, S.: JSACH 3 - The land component of the MPI Earth System Model: Documentation of version 3.2, Tech. Rep. 240, Max-Planck-Institut für Meteorologie, https://doi.org/10.17617/2.3279802, 2021.

Riemer, N.: Numerische Simulationen zur Wirkung des Aerosols auf die troposphärische Chemie und die Sichtweite, Ph.D. thesis, https://doi.org/10.5445/IR/2212002, fak. f. Physik, Diss. v. 15.2.2002 und Karlsruhe 2002. (Wissenschaftliche Berichte des Instituts für Meteorologie und Klimaforschung der Universität Karlsruhe. 29.), 2002.

Riemer, N., Ault, A. P., West, M., Craig, R. L., and Curtis, J. H.: Aerosol Mixing State: Measurements, Modeling, and Impacts, Reviews of Geophysics, 57, 187–249, https://doi.org/10.1029/2018RG000615, 2019.

Salzmann, M., Ferrachat, S., Tully, C., Münch, S., Watson-Parris, D., Neubauer, D., Siegenthaler-Le Drian, C., Rast, S., Heinold, B., Crueger, T., Brokopf, R., Mülmenstädt, J., Quaas, J., Wan, H., Zhang, K., Lohmann, U., Stier, P., and Tegen, I.: The Global Atmosphere-aerosol Model ICON-A-HAM2.3–Initial Model Evaluation and Effects of Radiation Balance Tuning on Aerosol Optical Thickness, Journal of Advances in Modeling Earth Systems, 14, e2021MS002 699, https://doi.org/10.1029/2021MS002699, 2022.

Seifert, A. and Beheng, K. D.: A two-moment cloud microphysics parameterization for mixed-phase clouds. Part 1: Model description, Meteorology and Atmospheric Physics, 92, 45–66, https://doi.org/10.1007/s00703-005-0112-4, 2006.

Seinfeld, J. H. and Pandis, S. N.: Atmospheric Chemistry and Physics: From Air Pollution to Climate Change, John Wiley & Sons, Inc., 2016.

Senior, C. A., Marsham, J. H., Berthou, S., Burgin, L. E., Folwell, S. S., Kendon, E. J., Klein, C. M., Jones, R. G., Mittal, N., Rowell, D. P., Tomassini, L., Vischel, T., Becker, B., Birch, C. E., Crook, J., Dougill, A. J., Finney, D. L., Graham, R. J., Hart, N. C. G., Jack, C. D., Jackson, L. S., James, R., Koelle, B., Misiani, H., Mwalukanga, B., Parker, D. J., Stratton, R. A., Taylor, C. M., Tucker, S. O., Wainwright, C. M., Washington, R., and Willet, M. R.: Convection-Permitting Regional Climate Change Simulations for Understanding Future Climate and Informing Decision-Making in Africa, Bulletin of the American Meteorological Society, 102, E1206 – E1223, https://doi.org/10.1175/BAMS-D-20-0020.1, 2021.

Siebesma, A. P., Bony, S., Jakob, C., and Stevens, B., eds.: Clouds and Climate: Climate Science's Greatest Challenge, Cambridge University Press, Cambridge, https://doi.org/10.1017/9781107447738, 2020.

Stevens, B., Satoh, M., Auger, L., Biercamp, J., Bretherton, C. S., Chen, X., Düben, P., Judt, F., Khairoutdinov, M., Klocke, D., Kodama, C., Kornblueh, L., Lin, S.-J., Neumann, P., Putman, W. M., Röber, N., Shibuya, R., Vanniere, B., Vidale, P. L., Wedi, N., and Zhou,

L.: DYAMOND: the DYnamics of the Atmospheric general circulation Modeled On Non-hydrostatic Domains, Progress in Earth and Planetary Science, 6, 61, https://doi.org/10.1186/s40645-019-0304-z, 2019.

500 Stier, P., Feichter, J., Kinne, S., Kloster, S., Vignati, E., Wilson, J., Ganzeveld, L., Tegen, I., Werner, M., Balkanski, Y., Schulz, M., Boucher, O., Minikin, A., and Petzold, A.: The aerosol-climate model ECHAM5-HAM, Atmospheric Chemistry and Physics, 5, 1125–1156, https://doi.org/10.5194/acp-5-1125-2005, 2005.

Stier, P., Seinfeld, J. H., Kinne, S., and Boucher, O.: Aerosol absorption and radiative forcing, Atmospheric Chemistry and Physics, 7, 5237–5261, https://doi.org/10.5194/acp-7-5237-2007, 2007.

505 Taylor, K. E., Williamson, D., and Zwiers, F.: The sea surface temperature and sea ice concentration boundary conditions for AMIP II simulations, Tech. Rep. 60, Lawrence Livermore National Laboratory, 2000.

Tegen, I., Neubauer, D., Ferrachat, S., Siegenthaler-Le Drian, C., Bey, I., Schutgens, N., Stier, P., Watson-Parris, D., Stanelle, T., Schmidt, H., Rast, S., Kokkola, H., Schultz, M., Schroeder, S., Daskalakis, N., Barthel, S., Heinold, B., and Lohmann, U.: The global aerosol–climate model ECHAM6.3–HAM2.3 – Part 1: Aerosol evaluation, Geoscientific Model Development, 12, 1643–1677,
510 https://doi.org/10.5194/gmd-12-1643-2019, 2019.

Textor, C., Schulz, M., Guibert, S., Kinne, S., Balkanski, Y., Bauer, S., Berntsen, T., Berglen, T., Boucher, O., Chin, M., Dentener, F., Diehl, T., Easter, R., Feichter, H., Fillmore, D., Ghan, S., Ginoux, P., Gong, S., Grini, A., Hendricks, J., Horowitz, L., Huang, P., Isaksen, I., Iversen, I., Kloster, S., Koch, D., Kirkevåg, A., Kristjansson, J. E., Krol, M., Lauer, A., Lamarque, J. F., Liu, X., Montanaro, V., Myhre, G., Penner, J., Pitari, G., Reddy, S., Seland, Ø., Stier, P., Takemura, T., and Tie, X.: Analysis and quantification of the diversities of aerosol
515 life cycles within AeroCom, Atmospheric Chemistry and Physics, 6, 1777–1813, https://doi.org/10.5194/acp-6-1777-2006, 2006.

Thornhill, G. D., Collins, W. J., Kramer, R. J., Olivié, D., Skeie, R. B., O'Connor, F. M., Abraham, N. L., Checa-Garcia, R., Bauer, S. E., Deushi, M., Emmons, L. K., Forster, P. M., Horowitz, L. W., Johnson, B., Keeble, J., Lamarque, J.-F., Michou, M., Mills, M. J., Mulcahy, J. P., Myhre, G., Nabat, P., Naik, V., Oshima, N., Schulz, M., Smith, C. J., Takemura, T., Tilmes, S., Wu, T., Zeng, G., and Zhang, J.: Effective radiative forcing from emissions of reactive gases and aerosols – a multi-model comparison, Atmospheric Chemistry and
520 Physics, 21, 853–874, https://doi.org/10.5194/acp-21-853-2021, 2021.

Vogel, A., Alessa, G., Scheele, R., Weber, L., Dubovik, O., North, P., and Fiedler, S.: Uncertainty in Aerosol Optical Depth From Modern Aerosol-Climate Models, Reanalyses, and Satellite Products, Journal of Geophysical Research: Atmospheres, 127, e2021JD035 483, https://doi.org/10.1029/2021JD035483, e2021JD035483 2021JD035483, 2022.

Watson-Parris, D., Schutgens, N., Reddington, C., Pringle, K. J., Liu, D., Allan, J. D., Coe, H., Carslaw, K. S., and Stier, P.: In situ constraints
525 on the vertical distribution of global aerosol, Atmospheric Chemistry and Physics, 19, 11 765–11 790, https://doi.org/10.5194/acp-19-11765-2019, 2019.

Wehr, T., Kubota, T., Tzeremes, G., Wallace, K., Nakatsuka, H., Ohno, Y., Koopman, R., Rusli, S., Kikuchi, M., Eisinger, M., Tanaka, T., Taga, M., Deghaye, P., Tomita, E., and Bernaerts, D.: The EarthCARE mission – science and system overview, Atmospheric Measurement Techniques, 16, 3581–3608, https://doi.org/10.5194/amt-16-3581-2023, 2023.

530 Zhang, K., O'Donnell, D., Kazil, J., Stier, P., Kinne, S., Lohmann, U., Ferrachat, S., Croft, B., Quaas, J., Wan, H., Rast, S., and Feichter, J.: The global aerosol-climate model ECHAM-HAM, version 2: sensitivity to improvements in process representations, Atmospheric Chemistry and Physics, 12, 8911–8949, https://doi.org/10.5194/acp-12-8911-2012, 2012.